PAPER

Check for updates

Fabrication of a self-assembled and vascularized tumor array *via* bioprinting on a microfluidic chip†

Gihyun Lee,[a] Soo Jee Kim[a] and Je-Kyun Park iD *[abc]

A tumor microenvironment (TME) is a complex system that comprises various components, including blood vessels that play a crucial role in supplying nutrients, oxygen, and growth factors, as well as delivering chemotherapy drugs to the tumor mass through the vascular endothelial barrier. To replicate the TME *in vitro*, several bioprinting and microfluidic organ-on-a-chip technologies have been developed. However, these technologies have not been fully exploited in terms of potential benefits of bioprinting and microfluidics, such as precise spatial control for biological samples, construction of multiple TMEs per microfluidic device, and the ability to adjust culture environments for better biological similarity. In addition, the complex transport phenomena within the vascular endothelial barrier and the aggregated tumor mass in the TME model should be considered before applying the model to drug treatment and screening. In this study, we describe a novel integrative technology that addresses these issues by introducing a self-organized TME array bioprinted on a microfluidic chip consisting of a vascular endothelial barrier surrounding breast cancer spheroids. To integrate the TME array onto the microfluidic platform, a microfluidic substrate for extrusion bioprinting was developed for a cell culture platform, which enables diffusivity control by microstructures and establishes a perfusion culture environment inside the culture channel. We also analyzed the cellular behaviors within the TME array to investigate the influence of the diffusivity on the self-organization process required to form the vascular endothelial barrier surrounding breast cancer spheroids.

Introduction

A tumor microenvironment (TME) comprises a diverse group of cells that are compartmentalized into functional units and interact with each other.[1] These tumor-associated cells surround the solid tumor tissue within a complex niche that facilitates cancer growth, metastasis, and cell–cell communication.[2,3] Blood vessels play a critical role in supplying cancer cells with oxygen, nutrients, and growth factors, as well as delivering chemotherapy drugs across the vascular endothelium.[4] The concentration of substances decreases exponentially over distance from the blood vessel,[5] as they diffuse through the extracellular matrix (ECM) before finally reaching the solid tumor. The dense aggregation of

tumor cells also impedes penetration into the core region of the microcompartmentalized tissue.[6] During drug treatment, drug molecules penetrate the core of the tumor tissue slowly, leading to drug resistance within the tissue.[7,8] Consequently, the complex transport phenomena within the TME are significantly influenced by the vascular barrier, ECM, and tumor mass.

To study the complex composition and transport phenomena of TMEs, creating bioengineered models capable of replicating this environment *in vitro* is required.[4,9,10] Among various biofabrication technologies that mimic complex microphysiological environments, including TMEs,[11–14] microfluidic organ-on-a-chip and bioprinting have been used to fabricate biologically relevant and reproducible *in vitro* models.[15–17] Microfluidic organ-on-a-chip offers several advantages for *in vitro* TME models, enabling researchers to precisely control culture environments, such as mechanical/chemical factors, cellular composition, and culture medium flow.[18–22] This allows for the replication of the complex microenvironment of tumor tissues in a biologically relevant and reproducible manner. However, spatial restrictions of microchannels limit the number of biological models per microfluidic device, as only one cell–hydrogel composition per microchannel can be introduced. On the other hand, bioprinting

[a] Department of Bio and Brain Engineering, Korea Advanced Institute of Science and Technology (KAIST), 291 Daehak-ro, Yuseong-gu, Daejeon 34141, Republic of Korea. E-mail: jekyun@kaist.ac.kr; Fax: +82 42 350 4310; Tel: +82 42 350 4315
[b] KAIST Institute for Health Science and Technology, 291 Daehak-ro, Yuseong-gu, Daejeon 34141, Republic of Korea
[c] KAIST Institute for the NanoCentury, 291 Daehak-ro, Yuseong-gu, Daejeon 34141, Republic of Korea
† Electronic supplementary information (ESI) available: Fig. S1–S3 and video S1. See DOI: https://doi.org/10.1039/d3lc00275f

enables the accurate deposition of cell-laden hydrogels, known as bioinks, at designated locations to facilitate prototyping devices without spatial restrictions.[23–26] However, for the creation of more complex and detailed TME models, further interfacing of bioprinted constructs with suitable cell culture and analysis systems is required.[27]

Several approaches have been developed to overcome the limitations of each technology using integrative technology of organ-on-a-chip and bioprinting.[17,28] This technology combines the advantages of both methods to create the next generation of biologically functional *in vitro* models, such as thick vascularized tissue-on-a-chip,[25] human glioblastoma-on-a-chip,[29] heart-on-a-chip,[30] and cardiac microphysiological devices.[31] Furthermore, a microfluidic substrate for bioprinting has been developed to micropattern low-viscosity bioinks with high-resolution by a capillary pinning effect for retaining the hydrogel structures.[32] To achieve more significant similarity in TME models, it is essential to employ reconstruction technologies that mimic tumor heterogeneity, model vasculature, and facilitate the formation of tumor spheroids.[33] Previous research has shown that endothelial cells can self-assemble to form a vascular barrier in the liquid–ECM interface, utilizing a combination of geometrical features, chemical gradients, and flow rates.[30,34,35] Moreover, when tumor cells with cell-to-cell and cell-to-matrix interactions are cultured in a hydrogel, they gradually aggregate to form spheroids representing the tumor mass.[36] By simultaneously self-organizing tumor and vascular endothelial cells in a single model, creating a TME model that closely mimics the tumor tissue and its environment would be possible. However, current technologies have not fully exploited the advantages of bioprinting and microfluidics, such as precise spatial control for biological samples, construction of multiple TMEs per microfluidic device, and adjustment of the culture environment for better biological similarity.

In this study, we present a novel approach to address these issues by printing a TME array on a microfluidic chip to create multiple TME models and self-organizing a vascular endothelial barrier surrounding tumor spheroids in each TME unit. The proposed system consists of multiple TME units, where each unit is capable of self-organization by regulating diffusivity using microstructures. Each TME unit contains a vascular endothelial barrier surrounding cancer spheroids, enabling the reconstruction of tumor heterogeneity, vasculature modeling, and tumor spheroid formation for better recreation of a TME model with respect to mass transport. We monitored and analyzed the behavior of breast cancer cells and vascular endothelial cells during a 7 day culture period within the TME array cultured under a dynamic medium flow to investigate the influence of the hydrogel geometry on spheroid formation and vascular barrier formation.

Experimental

Cell maintenance

Human umbilical vein endothelial cells (HUVECs; LONZA, Walkersville, MD, USA) were cultured in an endothelial growth medium (EGM-2; LONZA), and the cells at passages 3 to 5 were used for active cellular behavior. BT474 breast cancer cells (BT474; Korean Cell Line Bank, Seoul, Korea) were cultured in an RPMI-1640 medium (Gibco-Invitrogen, Carlsbad, CA, USA), including 10% fetal bovine serum and 1% penicillin–streptomycin. The culture medium of HUVEC and BT474 cells was exchanged every two or three days.

Cell–hydrogel bioinks and crosslinking agents

As a bioink, a hydrogel blend based on alginate and fibrin was used to induce self-organization of the vascular endothelial cells and breast cancer cells to recreate a TME, as shown in Fig. 1A. 1.0% RGD-alginate (NOVATACH MVG GRGDSP; Novamatrix, Sandvika, Norway) diluted in phosphate-buffered saline (PBS) and 5 mg mL^{-1} fibrinogen (bovine plasma origin; Sigma, Saint Louis, MO, USA) dissolved in PBS were prepared. Two hydrogel precursors were mixed in a 1 : 1 ratio to make the 0.5% RGD-alginate–2.5 mg mL^{-1} fibrinogen (Alg–Fib) blend. Using the blend, we prepared the bioink in which 2×10^6 BT474 cells and 5×10^6 HUVECs were suspended in 1 mL of Alg–Fib. 10% and 2% CaCl$_2$ (CaCl$_2$ dihydrate; Sigma) solutions diluted in deionized water were prepared for primary (aerosol type) and secondary (solution type) crosslinking of alginate of the bioink, respectively. 50 U mL^{-1} thrombin (Dongin Science, Daejeon, Korea) dissolved in PBS was prepared to transform the fibrinogen of the bioink into fibrin after alginate crosslinking steps. The hydrogel precursors and crosslinking solution were sterilized with a 0.2 μm filter.

Microfluidic substrate for extrusion bioprinting

A microfluidic substrate for extrusion bioprinting consisted of 200 μm high microchannels and microstructures capable of printing a 4 × 10 TME array with six micropillars per unit (Fig. 1B). When assembled with a clamping system, the microchannels were designed to support dynamic cell culture without leakage. Referring to our previous work,[37,38] the wall structure with a 1 mm width was intended in the microfluidic channel boundary to focus the pressing force. The pillar microstructures were applied to microfluidic organ-on-chip platforms to guide hydrogels.[39] In the proposed microfluidic substrate, the pillars were designed to trap small volumes of bioink, which was patterned into microstructures of uniform height and anchored the printed array in place during dynamic cell culture. The trapped hydrogel has six liquid–hydrogel interfaces that can not only supply the growth medium into the cells inside the hydrogel for mimicking the TME configuration but also provide the interfacing area for cell adhesion and diffusivity control. The microfluidic substrate was fabricated through soft lithography. To make the microstructures and microchannels of the substrate, a 200 μm high photoresist (SU-82100; MicroChem, Newton, MA, USA) layer was patterned on a silicon wafer following spin coating, baking, ultraviolet (UV) exposing, and developing steps. Poly(dimethylsiloxane)
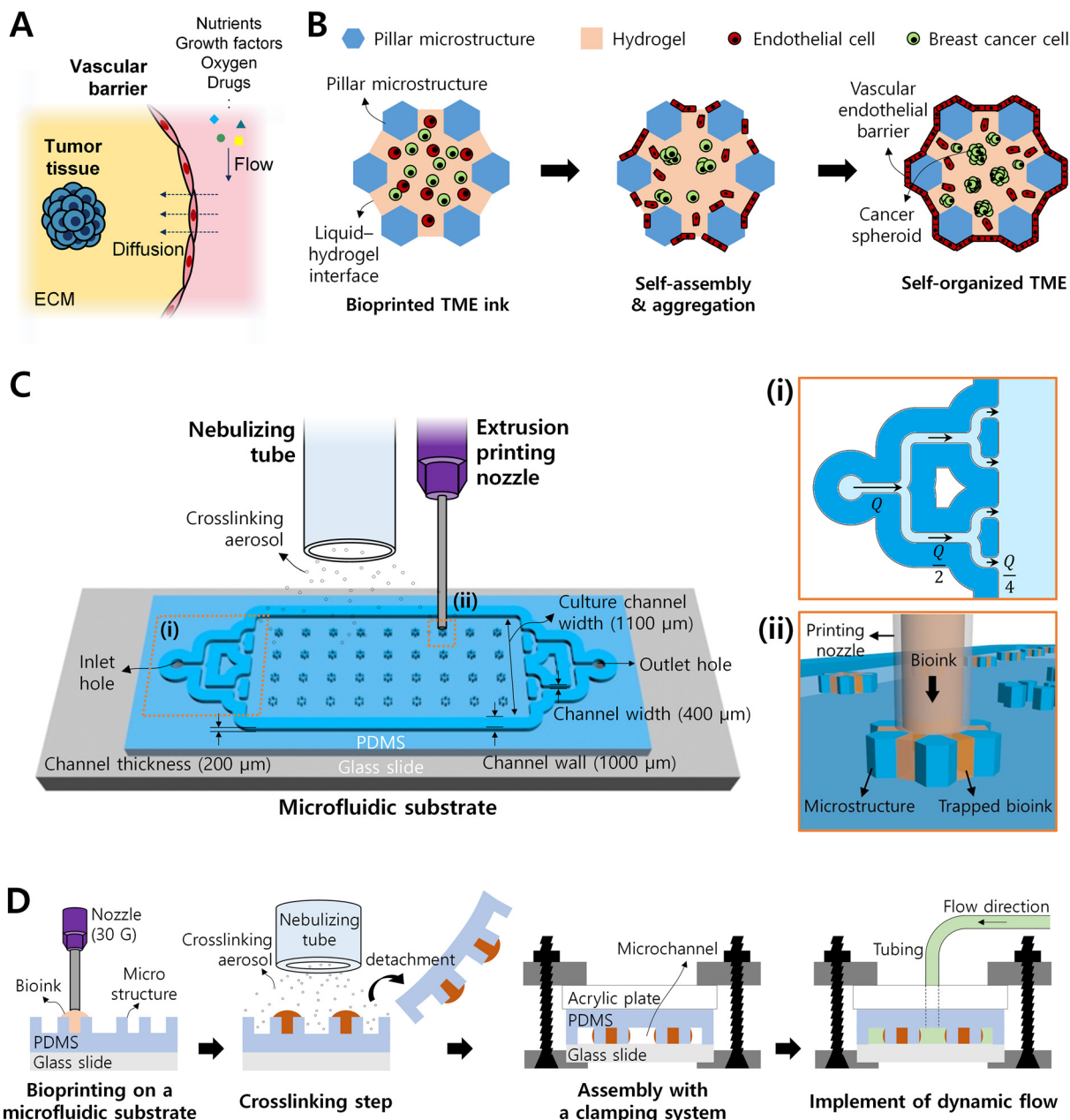
Fig. 1 Concept for self-organized TME array-on-a-chip through bioprinting on a microfluidic substrate. (A) Schematic of a TME, including cancer tissue, ECM, and vascular endothelial barrier. (B) Formation of the vascular barrier surrounding tumor spheroids in a TME unit, enabling self-organization of the cancer cells and vascular endothelial cells using microstructures. (C) Direct bioprinting of the TME array on a microfluidic substrate. (i) The fluid distribution channel to uniformly supply the growth medium into the array. (ii) The bioink trapped by microstructures to create the liquid–hydrogel interfaces in the TME unit. (D) Whole process from bioprinting to assembly for creating a microfluidic cell culture system.

(PDMS) (Sylgard 184; Dow Corning, Midland, MI, USA) was prepared by mixing a base and curing agent with a 10 : 1 ratio and pouring it on the SU-8 patterned wafer. After thermal curing at 65 °C for 2 h, the PDMS detached from the wafer was cut to use as a bioprinting substrate and punched on the inlet and outlet ports to implement a dynamic cell culture environment. Before bioprinting onto the substrate, the prepared substrates were sterilized at 121 °C for about 60 min using an autoclave.

Direct bioprinting on the microfluidic substrate

To fabricate multiple TMEs of various conditions on a single microfluidic device, a bioprinting system could stably coordinate a small-volume bioink at accurate locations without hydrogel evaporation during a printing process. In our previous work, we developed an extrusion-based bioprinter consisting of a bioprinting nozzle and a crosslinking aerosol tube installed on the 3D-printed

printhead.[23,40] In the current system, we replaced the only printing nozzle with a single barrel nozzle with 30-gauge and kept the crosslinking aerosol tube to stabilize the printing of small volumes of bioink and improve the printability minimizing the hydrogel drying issue. The finalized bioprinting system was set up to supply crosslinking aerosol during the printing process. The movement of the printhead was programmed using a GCode for a 4 × 10 array to precisely locate the small volume of bioink on the microfluidic substrate. Before starting the bioprinting, the microfluidic substrate was placed on the printing bed with the patterned side facing up. During the printing process, the extruded bioink was immediately exposed to a crosslinking aerosol of 10% $CaCl_2$ to crosslink the bioink and minimize bioink evaporation (Fig. 1C). After printing, the substrate was immersed in 2% $CaCl_2$ and 50 U mL^{-1} thrombin solution for secondary crosslinking sequentially (Fig. 1D). The microfluidic substrate, including the bioprinted array, was covered with a glass slide to create microchannels and then assembled with a clamping system by tightening screws and nuts to prevent fluid leakage during the cell culture period. We then introduced a 1 mL h^{-1} flow to establish a microfluidic cell culture environment with a stable flow without fluid leakage from the reversibly bonded interface between the microfluidic substrate and the glass slide.

Simulation for analysis of the flow characteristics inside the culture channel

We conducted a simulation for analyzing fluid dynamics, such as concentration distribution and flow velocity, using COMSOL Multiphysics 6.0 (COMSOL, Inc., Burlington, MA, USA) as finite element modeling software. To simulate fluid behavior inside the microfluidic cell culture system, the microfluidic substrate was designed with AutoCAD (AutoDesk, San Francisco, CA, USA) to draw the distribution channels (Fig. 1C, i), culture channel, and pillar microstructures (Fig. 1C, ii). The distribution and culture channels have 400 μm and 11 mm widths, respectively. The six pillar microstructures formed a 4 × 10 array as one unit. Each row (10 units) was designed with different pillar gaps of 25, 50, 100, and 150 μm. After designing the microfluidic substrate, the CAD file was then loaded and modeled with 200 μm height in COMSOL. In COMSOL software, two physics for the laminar flow and the transport of diluted species were used to set the flow environment and diffusion phenomena in the microchannel. The reference pressure level and reference temperature were set to 1 atm and 293.15 K, respectively. The fluid properties were used from water for a solution infilled and applied in the microchannel. All boundaries except the inlet and outlet were set as a wall, and the fluid was introduced with a flow rate of 1 mL h^{-1} into the inlet. The diffusion coefficient was set to 2×10^{-9} m^2 s^{-1} to approximate a small molecule in water inside the microchannel. In addition, the shear rate around the hydrogel units with different pillar gaps at various flow rates from 0.25 to 4 mL h^{-1} was investigated. Although the Alg–Fib hydrogel blend (0.5% RGD-alginate and 2.5 mg mL^{-1} fibrinogen) was used as the bioink in this study, we could not search the exact material properties, such as the porosity and diffusion coefficient of Alg–Fib, to create a reliable simulation model. The simulation model for visualizing the shear rate was simplified by setting the hydrogel region as a wall. The simulation was conducted with a time-dependent setting to analyze the concentration distribution and flow velocity at various time points.

Molecular diffusion into the hydrogel unit printed in the microfluidic cell culture system

The PBS solution with red food dye was prepared to confirm how long it would take to infill the fluid in the culture channel and supply the fluid into the whole array. During the introduction of the 1 mL h^{-1} solution through microchannels, we captured time-lapsed stereoscopic images of the entire 4 × 10 array in the microfluidic platform. In addition, to visualize the diffusion phenomena in a unit of the 4 × 10 array, we prepared a 1 μM 10 kDa FITC–dextran (FD10S; Sigma) solution dissolved in PBS. After the FITC solution was supplied to a 4 × 10 hydrogel array integrated with a microfluidic cell culture system at a 1 mL h^{-1} flow rate, the diffusion phenomena in a unit of the array were observed on a digital fluorescence microscope (F1-CIS; Nanoscope Systems, Daejeon, Korea) and captured to obtain time-lapsed images for 30 min. The fluorescence intensity of FITC–dextran diffused into each hydrogel was measured along a line inside the hydrogel, and the line profile over diffusion time was analyzed with ImageJ software (https://imagej.nih.gov/ij/). In addition, to analyze the barrier function of the vascularized and self-assembled TME models, the EGM-2 medium containing 1 μM FITC–dextran (10 kDa) was introduced into the TME array at a flow rate of 1 mL h^{-1}. The time-lapse fluorescence images were captured over diffusion time, and the fluorescence intensity in the region of the hydrogel core was measured from the images to compare the diffusivity in the four TME groups.

Cell viability test

Cell viability was calculated by staining the nuclei of the total and dead cells with a live/dead staining kit (ReadyProbes™ cell viability imaging kit, blue/green; Invitrogen, Waltham, MA, USA). The live reagent and dead reagent were prepared by mixing two drops of each staining solution per 1 mL culture medium, by following the manual from the manufacturer. The staining solution was loaded into the sample and placed in a 37 °C incubator for 30 min. After staining, the fluorescence image was captured, and the viability was analyzed by calculating the ratio of the area of the total cells' nuclei and dead cells' nuclei from the image on ImageJ.

Immunostaining of the TME construct for imaging

The TME constructs were fixed with 4% formaldehyde for 30 min for staining human growth factor receptor 2 (HER2), CD31, and nuclei of the BT474 cells and HUVECs. The TME construct was washed with PBST (0.1% PBS–Tween) and treated with a blocking solution (1% bovine serum albumin, 10% normal goat serum, and 0.3 M glycine in 0.1% PBS–Tween) for 1 h at room temperature. After washing three times, the TME construct was sequentially stained with a Fluor-488 conjugated HER2 antibody (ab275994; AbCam, Waltham, MA, USA) diluted to 1/100 and a Fluor-647 conjugated CD31 antibody (ab215912; AbCam) diluted to 1/100 overnight at 4 °C for staining the BT474 cells and HUVECs, respectively. The nuclei of the BT474 cells and HUVECs were stained with Hoechst 33342 (62 249; Thermo Fisher, Norcross, GA, USA) for 30 min. After washing three times, the samples were submerged in Dulbecco's phosphate-buffered saline (DPBS) and captured on a digital fluorescence microscope (F1-CIS; Nanoscope Systems) and a confocal microscope (LSM 880; LSM 980; Carl Zeiss, Jena, Germany) of KAIST Analysis Center for Advancement (KARA) for analysis of the TME construct.

Analysis of self-organization of the vascular endothelial barrier surrounding breast cancer spheroids

The HUVEC barrier in the various hydrogel patterns was analyzed by staining with CD31. To quantify HUVEC barrier formation, we calculated the HUVEC barrier formation rate by counting the HUVEC barriers covered in the six liquid–hydrogel interfaces of each unit on days 3 and 7 of culture. To analyze the breast cancer spheroid formation in the various hydrogel patterns, the HER2 expression was used for recognizing the BT474 cells in the TME model and obtaining the cell growth images on days 3 and 7 of culture. The area of the aggregated BT474 cells was measured from the HER2-expressed region at culture days 3 and 7 on ImageJ. The single BT474 cells were excluded from the analysis of spheroid formation. The images of the self-organized vascular barrier–tumor spheroid unit were observed from the fluorescence microscope and confocal microscope. In addition, to compare the experimental results with a standard 3D culture platform, the BT474 cells and HUVECs were cultured three-dimensionally in the 96-well plate and the cellular behaviors were observed at days 3 and 7 with the same immunostaining conditions. In order to prepare a control model, the BT474 cells (2×10^6 cells per mL) and HUVECs (5×10^6 cells per mL) were mixed in the Alg–Fib hydrogel blend and loaded in the 96-well plate. After sequential crosslinking with 2% CaCl$_2$ and 50 U mL^{-1} thrombin solution, the cells were cultured in EGM-2, and the model was observed.

Statistical analysis

All data in the bar plots were represented as average ± standard deviation. To evaluate the statistical significance of the biological results, statistical analysis was conducted using the Kruskal–Wallis test with Dunn's *post hoc* multiple comparison test on the IBM SPSS Statistics. The p-values of <0.05 (*), <0.01 (**), and <0.001 (***) were considered statistically significant.

Results and discussion

Direct bioprinting of the hydrogel array on the microfluidic substrate

To recreate a TME comprised of a tumor mass and vascular barrier, a self-organization technology was needed to facilitate the formation of a vascular endothelial barrier surrounding tumor spheroids, as shown in Fig. 1A. While the underlying mechanism remains undisclosed, it is well-known that vascular endothelial cells, such as HUVECs, have an intrinsic property of forming a vascular barrier at the liquid–ECM interface by migrating towards a chemogradient.[30] In addition, BT474 cells can form a spheroid through gradual aggregation in 3D culture environments with sufficient growth medium.[36] Fig. 1B shows the process of self-organization of HUVECs and BT474 cells cultured in our bioprinted TME model. We hypothesized that the pillar microstructures will not only induce the formation of the HUVEC barrier by creating a liquid–hydrogel interface with a capillary pinning effect, but also regulate the formation of the BT474 spheroid by controlling diffusivity in the hydrogel *via* the pillar gaps. To integrate the TME models into a single microfluidic system as an array unit, we exploited a microfluidic substrate for extrusion bioprinting, as depicted in Fig. 1C. The microfluidic substrate was designed with microfluidic circuits (for fluid distributors and a cell culture channel), channel wall structures (for effective pressure-based assembly), and pillar microstructures (for bioink trapping and patterning as shown in Fig. 1B). A detailed overview of the entire process from bioprinting to device assembly is presented in Fig. 1D.

To fabricate the microfluidic substrate, a soft lithography process was employed to replicate a PDMS structure from a 200 μm high SU-8 patterned Si wafer (Fig. 2A). However, it was observed that the PDMS pillar microstructures were prone to tearing when detaching the PDMS from the SU-8 patterned wafer for microchannel patterns exceeding 200 μm, due to the high aspect ratio of the pillars. To achieve simultaneous extrusion of the bioink and crosslinking of the extruded material with aerosol, a printhead was modified with a printing nozzle and a nebulizing tube, as shown in Fig. 2B. The microfluidic substrate was placed on a bioprinting bed, and 4 × 10 array printing was initiated, as shown in Fig. 2C. To test the printing process, 2% alginate ink was printed under 10% CaCl$_2$ aerosol to localize the ink to the 4 × 10 array, which was then covered with a glass slide to create microchannels. Upon imaging the printed alginate array before the secondary crosslinking step, it was observed that the 4 × 10 alginate array was precisely printed on the designated location without the drying issue (Fig. 2D).
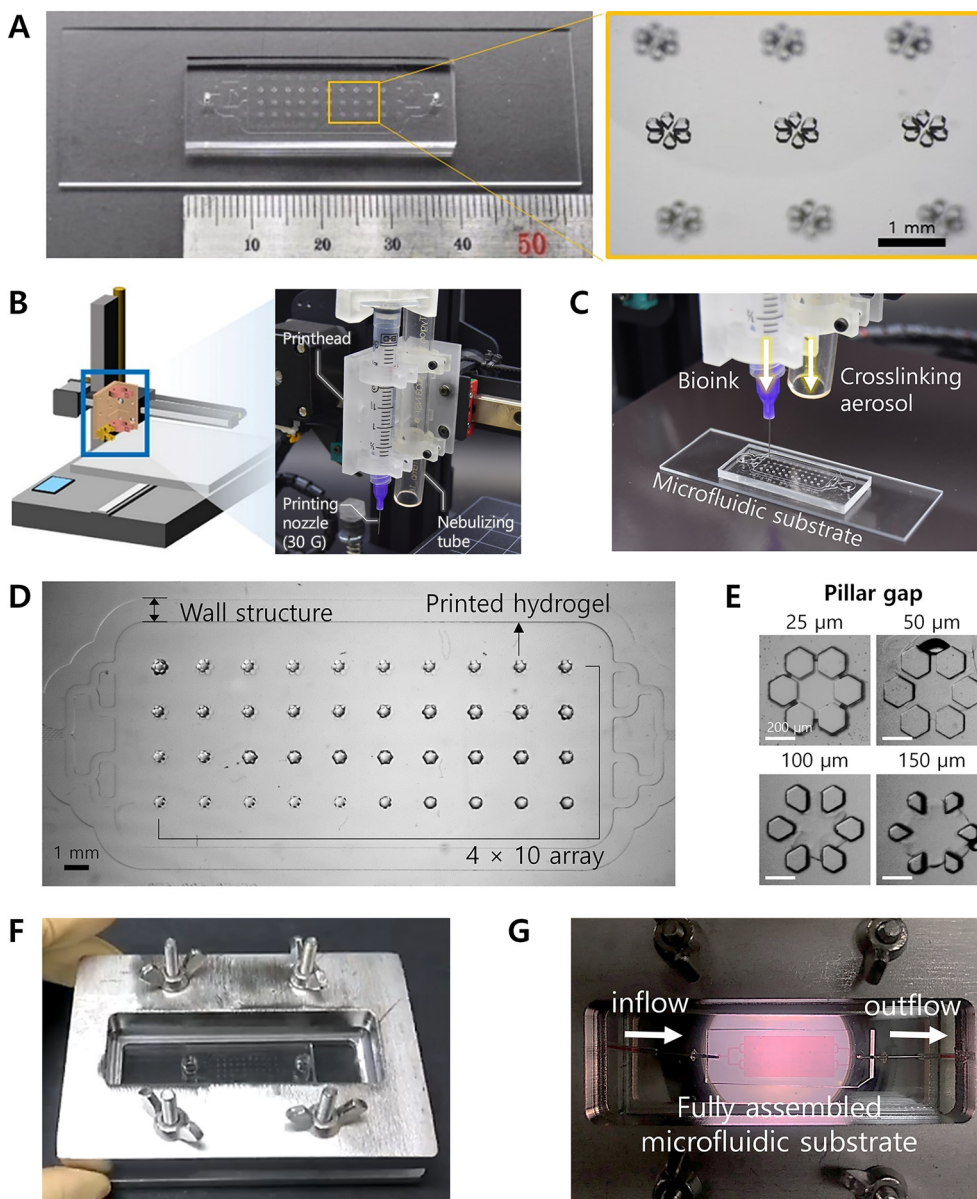
Fig. 2 Direct bioprinting of the hydrogel array on a microfluidic substrate for extrusion bioprinting. (A) A microfluidic substrate for extrusion bioprinting fabricated with soft lithography using PDMS. (B) The bioprinting system to supply crosslinking aerosol during the printing process. (C) Direct bioprinting on the microfluidic substrate. (D) A 4 × 10 hydrogel array printed on the microfluidic substrate following the pre-designed command. (E) Each hydrogel unit accurately printed and trapped by pillar microstructures with various designs. Fully assembled microfluidic substrate using (F) a clamping system for pressure-driven reversible bonding and (G) tubing for supplying fluid into the microchannel.

Furthermore, each alginate unit of the printed array was successfully trapped by the capillary pinning effect between the pillar microstructures with four different designs (Fig. 2E). Subsequently, the microfluidic substrate, including the hydrogel array, was subject to a secondary crosslinking step with 2% $CaCl_2$ solution and 50 U mL^{-1} thrombin solution sequentially. After fully crosslinking the hydrogel, the substrate was covered with a glass slide and assembled with a clamping system to introduce fluids (Fig. 2F). However, the use of this clamping system for reversible bonding is susceptible to leakage when supplying fluid into the microchannel. To address this issue, we utilized a

channel wall structure that can focus the pressing force on a selective area of the microfluidic channel, as previously reported.[37,38] When the fluid was supplied into the channel at a flow rate of 1 mL h^{-1}, we confirmed that the red dye solution flowed without any leakage, as shown in Fig. 2G.

Flow characteristics inside the cell culture channel

The fluid dynamics in the microfluidic system were analyzed to confirm a uniform supply of growth medium to all array units and diffusion inside the hydrogel unit during dynamic culture. To visualize fluid behaviors, a red food dye solution
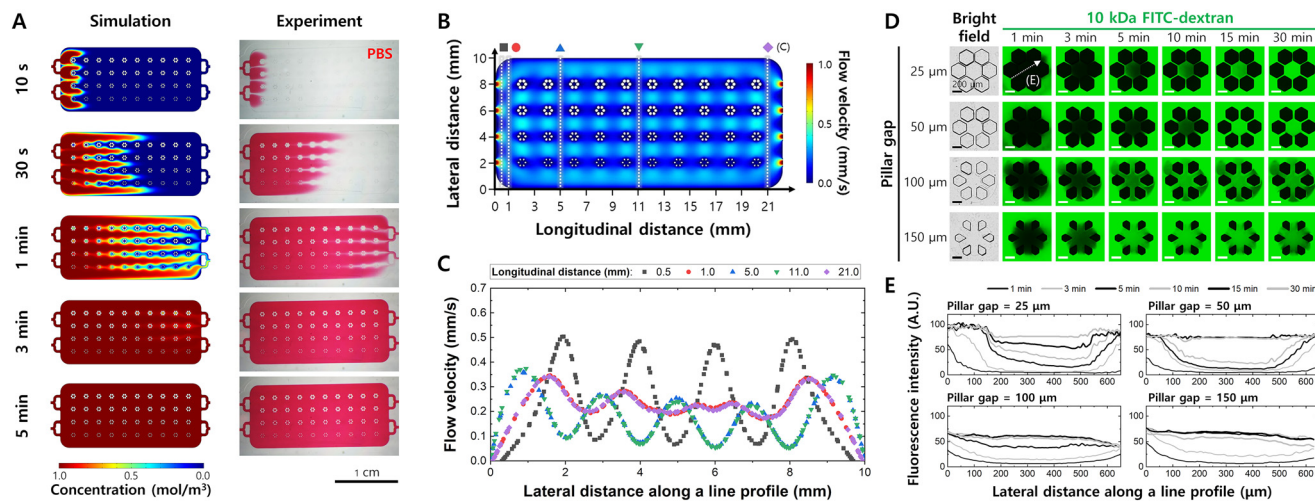
Fig. 3 Fluid flow characteristics inside the culture channel of the microfluidic system. (A) Concentration distribution in the cell culture channel when introducing a red dye solution with a 1 mL h^{-1} flow rate. (B) Simulation result for visualizing a flow velocity inside the cell culture channel in the flow condition. (C) Flow velocity profile at distances of 500, 1000, 5000, 11 000, and 21 000 μm from the inflow point. (D) Time-lapse images of 10 kDa FITC–dextran diffused into the hydrogel of various pillar gaps. (E) Concentration profiles of the FITC–dextran diffused inside the hydrogel over time.

was introduced at a flow rate of 1 mL h^{-1} into the microchannel filled with PBS solution. The red dye solution was distributed into four microchannels to supply the solution uniformly, and then all array units in the cell culture channel were gradually exposed to the red dye solution over time and completely filled within 5 min (Fig. 3A). The experimental concentration distribution was found be comparable to the simulation results. The flow velocity inside the culture channel was observed to decrease rapidly as the liquid supplied from the fluid distribution channels flowed to the wider culture channel (Fig. 3B). Specifically, the flow velocity decreased from 1 mm s^{-1} at the inflow point (end of the distribution channel) to 0.2–0.3 mm s^{-1} near the hydrogel unit (Fig. 3C). The results demonstrated that the introduced fluid could be supplied to the whole array unit within 5 min and that similar fluid characteristics could be implemented inside the cell culture channel. In addition, the shear rate occurring around the pillar microstructures when introducing the fluid with the different flow rates from 0.25 to 4 mL h^{-1} was observed through simulation (ESI,† Fig. S1). The relatively higher shear rate occurred around the hydrogel unit. The shear rate was higher at the liquid–hydrogel interfaces, where the fluid flowed faster. As the fluid with the larger flow rate was introduced, the shear rate was higher. Although the shear rate by the pillar gap was not significantly different, a high shear rate was observed at the location closer to the liquid–hydrogel interface as the pillar gap was wider.

A diffusion test was conducted to investigate molecular diffusion into a single hydrogel unit using a 10 kDa FITC–dextran solution with a similar molecular weight to growth factors. When a 10 kDa FITC–dextran solution was supplied to the cell culture channel, the dextran molecules diffused into the hydrogel through the liquid–hydrogel interfaces

between pillar microstructures. The saturation point for molecular diffusion in all hydrogel geometries was confirmed to reach within 30 min (Fig. 3D). In the pillar gap of 25 μm, the FITC–dextran molecules showed slower diffusion phenomena as the molecules penetrated through narrow interfaces between micropillars. The larger the interface, the faster the molecular diffusion and the shorter the saturation time. When measuring the fluorescence intensity along a line profile inside the hydrogel unit, FITC–dextran in each pillar gap group of 25, 50, 100, and 150 μm was saturated at approximately 30, 15, 10, and 5 min, respectively (Fig. 3E). Based on the results of the analysis of flow characteristics in the microfluidic system and single hydrogel units, we verified that all array units located in the cell culture channel were exposed to uniform culture conditions within 30 min of fluid supply, and the diffusion phenomena could be controlled by changing the liquid–hydrogel interfaces between pillar microstructures.

Biocompatibility for microfluidic cell culture

Before examining cellular behavior, we analyzed the biocompatibility of the microfluidic system and the bioprinted TME array under a dynamic flow. We also compared the viability of cells cultured in hydrogels with different sizes of the liquid–hydrogel interfaces. The TME bioink, which consisted of BT474 cells and HUVECs in a 0.5% RGD-alginate and 2.5 mg mL^{-1} fibrinogen blend, was directly bioprinted onto the microfluidic substrate using a printing nozzle under 10–15 mbar pneumatic pressure and crosslinked with 10% CaCl$_2$ aerosol during printing. We successfully located 40 TME dots (4 × 10 array) at the designated location in the culture channel, assembled with a clamping system, as shown in Fig. 4A. The bioprinted TME
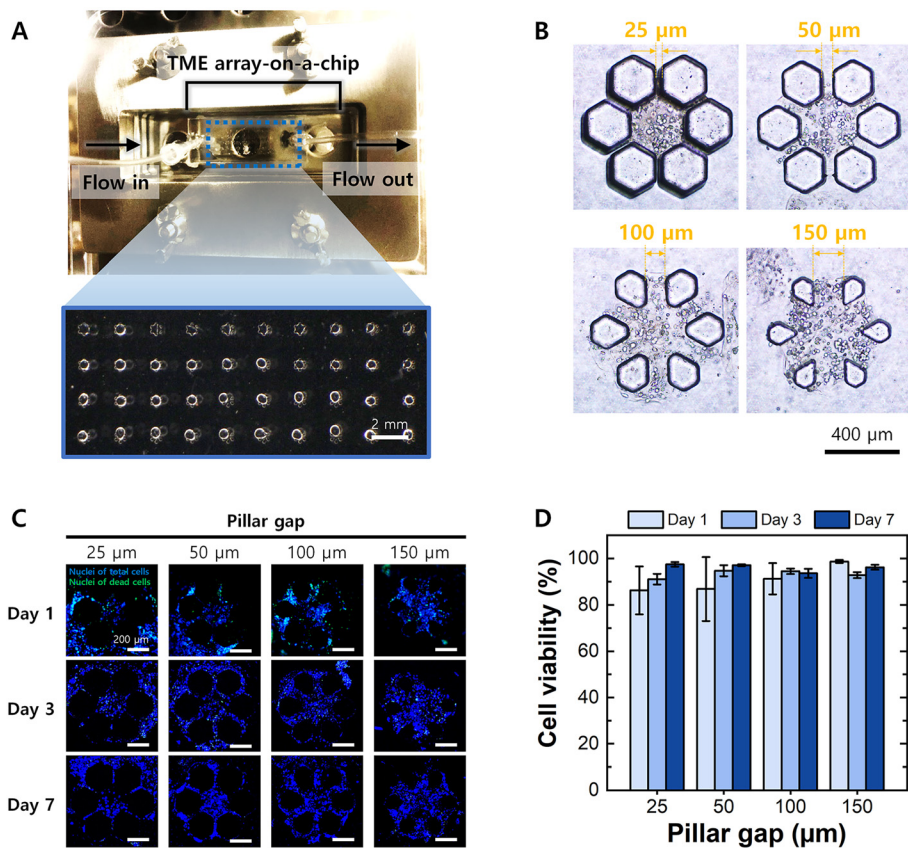
Fig. 4 Viability of the cells cultured in the bioprinting-based TME array-on-a-chip. (A) A TME array-on-a-chip for microfluidic cell culture. (B) The TME units in four different pillar gaps after bioprinting using TME bioink (BT474 cells and HUVECs suspended in an alginate–fibrinogen hydrogel precursor blend). (C) Live/dead assay indicating nuclei of total (blue) and dead (green) cells in the TME units of four pillar gap groups at 1, 3, and 7 days of culture. (D) Cell viability plot over the pillar gaps and culture times.

array was completely crosslinked with a 2% $CaCl_2$ solution and a 50 U mL^{-1} thrombin solution for 5 min each. Fig. 4B shows the bioinks trapped by micropillars with various gaps of 25, 50, 100, and 150 μm. To supply a growth medium to the cells, EGM-2 was introduced into the microfluidic system at a flow rate of 1 mL h^{-1}. The BT474 cells and HUVECs co-cultured under a dynamic flow were analyzed for biocompatibility in the culture environment for seven days. Viability analysis was also conducted on days 1, 3, and 7 in the bioprinted TME array to confirm the biocompatibility of the bioprinting process, microfluidic system, and dynamic culture environment.

The results showed that the group with a narrow interface of 25 μm pillar gap had a relatively large number of dead cell nuclei compared to the group with a wide interface of 150 μm pillar gap on the first day of culture (Fig. 4C). Although the cells cultured in TME groups with 25 and 50 μm pillar gaps showed relatively lower viability around 80% on day 1, the viability gradually increased above 90% during the seven days of culture (Fig. 4D). In contrast, the groups with 100 and 150 μm pillar gaps showed high cell viability from the first day, and the variation of the viability decreased as the pillar gap became wider. From the previous results in Fig. 3D, we indirectly confirmed that the growth medium supplied to the

cells would differ based on the size of the liquid–hydrogel interfaces. For this reason, the observed differences in viability may be attributed to the size of the liquid–hydrogel interface, which affects the diffusivity of the growth medium. Despite the initial differences in viability and different recovery tendencies in each group, the microfluidic system operated well as a biocompatible cell culture platform. Our findings confirm that the pillar gaps can affect the supply of the growth medium through liquid–hydrogel interfaces between the pillar microstructures and that all four designs can provide a suitable cell culture environment.

Self-organized TME array cultured in the microfluidic system

After confirming the biocompatibility of the culture system, we determined the influences of liquid–hydrogel interfaces to induce the self-organization in the TME cultured in the microfluidic system. Fig. 5A shows the 40 TME models cultured for seven days under a perfusion flow on the single microfluidic device. Despite the perfusion flow supplying the culture channel, the pillar microstructures stably held the TME units in place throughout the culture period and prevented the TME unit from being detached by the flow. The TME units were immunostained in the microfluidic
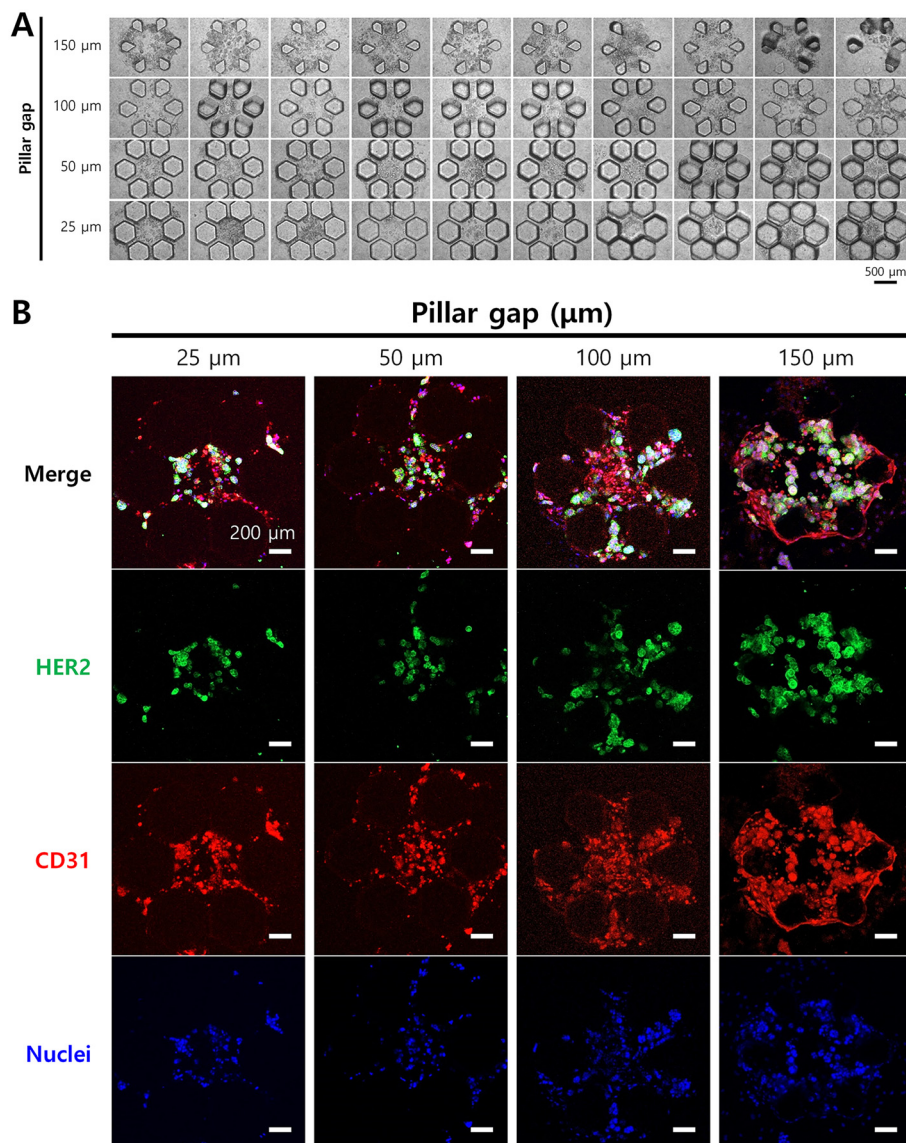
Fig. 5 TME array on a microfluidic cell culture system. (A) Microscope image of 40 TME units of a 4 × 10 array in the single microfluidic cell culture system. (B) The fluorescence images of the TME units immunostained in the microfluidic system with HER2 (green for observing aggregation of BT474 cells) and CD31 (red for observing self-assembly of HUVECs) to compare the four pillar gap groups.

system after day 7 to analyze the cellular characteristics of BT474 cells and HUVECs inside the hydrogel. The TME array was fixed and immunostained with HER2, CD31, and Hoechst to visualize the BT474 cells, HUVECs (especially their tight junctions), and nuclei of total cells, respectively. As shown in Fig. 5B, the TME units could be immunostained in the microfluidic system. The immunostained TME units exhibited the self-organization of the BT474 cells and HUVECs co-cultured in the four different hydrogel designs. In the 25 and 50 μm pillar gap groups, HER2 (green fluorescence) and CD31 (red fluorescence) were mostly observed in the center area of the TME unit. Although these groups slowly provided the culture medium through the narrow gap between pillar microstructures, the BT474 cells were still able to grow and aggregate in the hydrogel. On the

other hand, some HUVECs were observed between pillars since the HUVECs are smaller than BT474 cells. The vascular endothelial tight junction in the liquid–hydrogel interface was not observed in the 25 and 50 μm gap groups. This indicates that the narrow pillar gap groups were able to provide a culture environment for cell growth in the hydrogel, but it is difficult to form the HUVEC barrier on the liquid–hydrogel interfaces because the hydrogel wall in the interface does not provide a large enough area to adhere HUVECs. However, as the pillar gap widened, the TME unit showed more largely aggregated BT474 cells inside the hydrogel and more actively endothelialized HUVECs at the liquid–hydrogel interfaces. In particular, more BT474 cells and HUVECs as well as the HUVEC boundary were observed at the liquid–hydrogel interfaces of the 150 μm pillar gap

group. In this group, the vascular endothelial tight junction showed a clear boundary on the interfaces of the TME unit, indicating the presence of a vascular endothelial barrier surrounding the BT474 spheroids. This was achieved through the intrinsic property of HUVECs to move towards the liquid–ECM interface for taking higher nutrient concentrations, resulting in the self-organization of the TME to form the HUVEC barrier surrounding BT474 spheroids.

As a result, a TME array of 40 models (four groups of ten models per group) was successfully integrated onto a microfluidic cell culture system. The BT474 cells and HUVECs in the TME models exhibited diverse self-organization patterns, which could be modulated by controlling the molecular diffusion through the pillar microstructures. The cells exhibited different characteristics in terms of spheroid formation inside the hydrogel and vascular boundary formation on the liquid–hydrogel interface, depending on the pillar gap. Cellular behaviors were more pronounced when the exchange of the cell growth medium was smoother. Moreover, to form the HUVEC barriers in the liquid–hydrogel interfaces, a large enough area of the trapped hydrogel wall should be provided to adhere HUVECs. In the group with the widest pillar gap, we were able to observe the clear HUVEC boundary surrounding the BT474 spheroids on the TME array-on-a-chip.

Analysis of self-organization for the vascular endothelial barrier surrounding breast cancer spheroids in the TME array-on-a-chip

In order to quantify the cellular behaviors in response to different pillar gaps, we observed the self-organization of BT474 cells and HUVECs into a compartmentalized breast cancer spheroid–vascular barrier construct, which served as a representative model of the TME. During the culture period, we quantified the size of the BT474 spheroids and the HUVEC barrier formation rate inside the hydrogel and on the liquid–hydrogel interfaces of the TME unit. HER2 and CD31 immunostaining of the printed TME constructs after three and seven days of culture confirmed the formation of BT474 spheroids and HUVEC barriers within the TME unit over time. Fluorescence microscopic images of the HER2-expressed TME unit revealed that the BT474 cells gradually aggregated inside the hydrogel, leading to an increase in spheroid size (Fig. 6A). To quantitatively analyze the spheroid formation, we measured the HER2-expressed region, representing the aggregated BT474 cells. While the area of the BT474 spheroids increased over time in all four pillar gap groups, the trend varied (Fig. 6B). In the 25, 50, and 100 μm groups, the spheroid size increased as the pillar gaps widened, because the culture medium is more actively exchanged in the wider gap group. However, in the 150 μm pillar gap group, the spheroid area was similar to that of the 100 μm group on both days 3 and 7. This suggests that the difference in molecular diffusion between the 100 and 150 μm pillar gaps is not significant in supplying the growth

medium to the cells and forming spheroids in the TME construct. The BT474 cells were effectively aggregated in the pillar gap groups of 100 μm or wider, leading to the formation of the breast cancer spheroids inside the TME construct.

CD31 was immunostained to evaluate the formation of HUVEC barriers in the breast cancer spheroid–vascular barrier TME unit. A lot of HUVECs cultured for seven days were observed at the edge of the hydrogel, and we were able to confirm that they eventually formed an endothelial barrier on the liquid–hydrogel interfaces between the pillars. An orthogonal confocal image showed the HUVEC barrier on the liquid–hydrogel interface of the TME construct (Fig. 6C), and the tight junction boundary of the TME construct was observed in the top view image of the 150 μm pillar gap group. In the side view images following the a–a′, b–b′ and c–c′ lines of the top view image, it was confirmed that the HUVECs completely covered the entire hydrogel walls in the interface from the bottom to the ceiling of the microchannel. The barrier formation rate on the interfaces of one TME unit was quantitatively analyzed to compare the HUVEC barrier formation affected by the pillar gap (Fig. 6D). Although the barrier formation rate tended to increase over the culture time in all groups, the HUVEC barrier could be formed more rapidly as the pillar gap widened. In the widest group with a gap of 150 μm, the barrier formation rate on the liquid–hydrogel interface reached approximately 70% after three days of culture and increased to above 80% on day 7. The 100 μm gap group showed a 40% barrier formation rate on day 3 and increased to 80% on day 7, similar to the 150 μm gap group. However, the HUVECs cultured in the narrow groups with gaps of 25 μm and 50 μm were relatively slow to form the vascular barrier. The wider liquid–hydrogel interface could not only supply enough growth medium to the cells, but also provide a large area to adhere HUVECs, effectively forming the HUVEC barrier on the interface of the 100 μm or wider gap.

We observed the self-organization of BT474 cells and HUVECs in the TME construct and confirmed the behaviors of the cells depending on the pillar gap. In the widest group with a pillar gap of 150 μm, the TME construct was completely self-organized on day 7 of culture. A confocal image magnified in the liquid–hydrogel interface (Fig. 6E) showed that the BT474 cells were aggregated in the hydrogel area to form spheroids, while the HUVECs self-assembled on the interface to form a vascular barrier. The side view image on the *YZ* plane clearly indicated the adherence of HUVECs to the trapped hydrogel wall and coverage of the interface. As can be seen in the Z-projection image (Fig. 6F) and the Z-stack video (ESI,† Video S1), the BT474 spheroids were distributed within the hydrogel construct surrounded by a HUVEC barrier. Such a TME construct showing the HUVEC barrier surrounding BT474 spheroids could not be observed in the conventional culture system. In the control model cultured three-dimensionally in the 96-well plate, as shown in Fig. S2A (ESI†), the aggregated BT474 cells were observed inside the hydrogel on days 3 and 7 (ESI,† Fig. S2B). However,
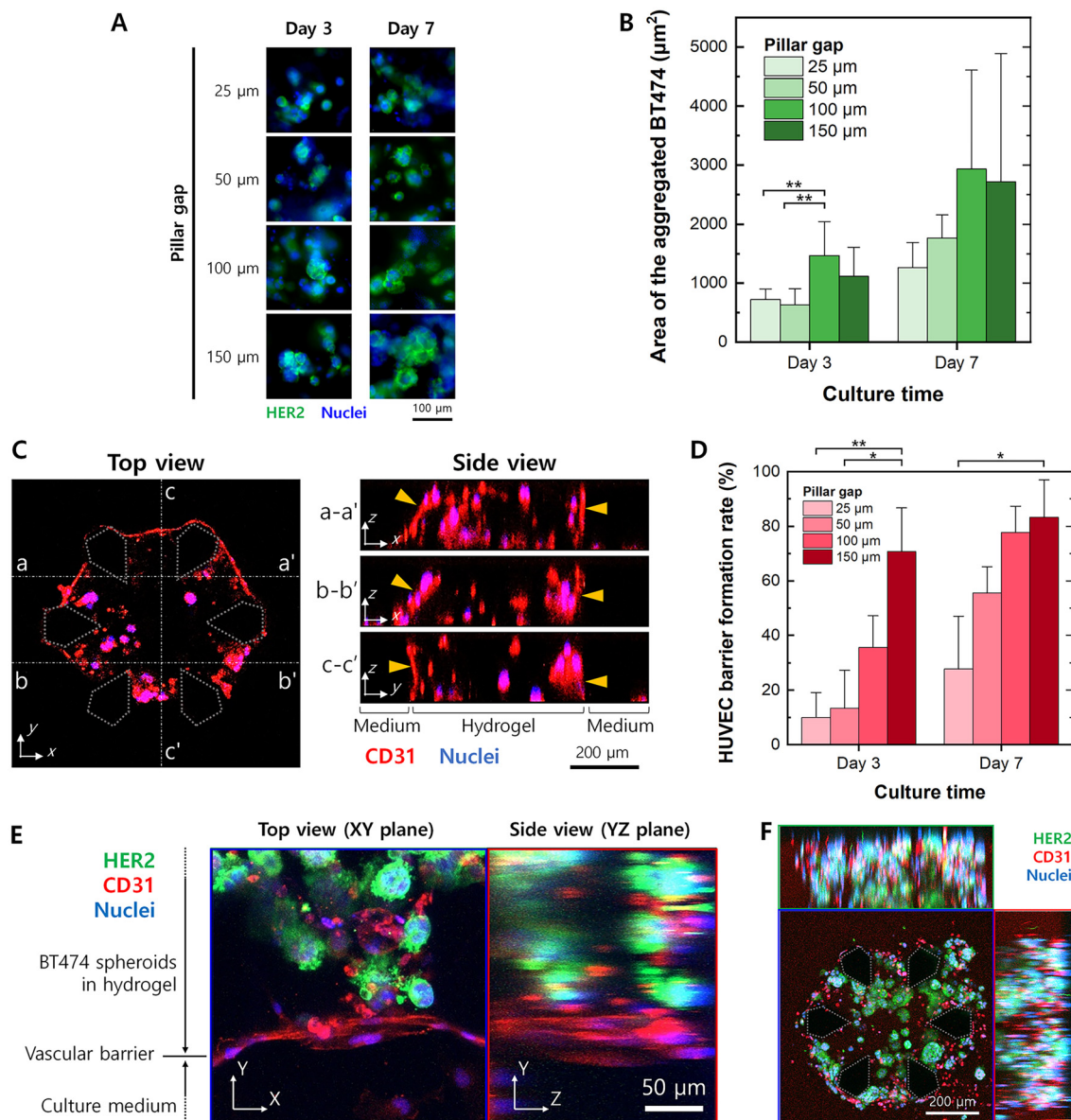
Fig. 6 Self-organization of the BT474 cells and HUVECs cultured in the bioprinted TME-on-a-chip. (A) Time-lapse immunostaining images for observing HER2 (green) expression in the TME units for analyzing the spheroid formation of the BT474 cells cultured in the various groups of pillar gap. (B) Quantitative analysis of the size of the aggregated BT474 cells over culture time. (C) Immunostaining image for observing vascular endothelial barriers showing CD31 (red) expressed from the HUVECs. The side view images observed along lines a-a', b-b', and c-c' of the top view image show the HUVEC barriers. The yellow arrows indicate the barriers. (D) Quantitative analysis for the vascular barrier formation of the HUVECs cultured in the various groups of pillar gap at 3 and 7 days of culture. (E) A magnified image of the self-organized TME showing the HUVEC barrier (CD31, red) surrounding BT474 spheroids (HER2, green) in the liquid–hydrogel interface. (F) An immunostaining image of the self-organized TME unit. The significant differences between the pillar gap groups were analyzed using the Kruskal–Wallis test with a *post hoc* Dunn's multiple comparison test. * $p < 0.05$, ** $p < 0.01$, *** $p < 0.001$.

the HUVECs did not self-assemble on the liquid–hydrogel interface and the vascular barrier was not observed during the culture period. These results confirmed that the proposed culture system outperformed the conventional culture system in accurately mimicking the TME.

To verify the barrier function of the vascularized and self-assembled TME model, the FITC–dextran medium was introduced into the TME array on the microfluidic device. The FITC–dextran molecules diffused more rapidly into the

TME unit as the pillar gap was wider (ESI,† Fig. S3A). In addition, the wider pillar gap group showed a faster saturation time point (ESI,† Fig. S3B). In the TME models with 25, 50, 100, and 150 μm gaps, FITC–dextran reached a steady state at about 40, 20, 15, and 10 min, respectively. In particular, in the 150 μm pillar gap group where the HUVEC barrier was best self-assembled, the barrier functionality was confirmed by comparing the hydrogel model without cells. At 5 min after the introduction of the FITC–dextran medium,

the hydrogel group without cells reached a steady state, but the hydrogel surrounded with the HUVEC barrier showed slower diffusion because the fluorescence molecules should pass through the vascular endothelial barrier (ESI,† Fig. S3C). From the results, we could confirm the barrier function of the HUVECs covered in the entire liquid–hydrogel interface. Using a microfluidic substrate for extrusion bioprinting, we were able to successfully fabricate a self-organized vascular endothelial barrier surrounding breast cancer spheroids in the TME array-on-a-chip.

Conclusions

We have successfully developed a self-organized TME array-on-a-chip using a microfluidic substrate for extrusion bioprinting, which consists of a vascular endothelial barrier surrounding breast cancer spheroids. The microfluidic substrate features microchannels, wall structures, and pillar microstructures, which facilitate the stable printing of a small-volume bioink array and the assembly of microchannels to supply the growth medium to the cells without fluid leakage. The microfluidic cell culture system exhibited high viability of BT474 cells and HUVECs for up to seven days of culture under medium flow. The pillar microstructures played a crucial role in trapping the bioink during bioprinting and providing a controlled culture environment. By controlling the different sizes of the gap between the pillar microstructures, we were able to induce the self-organization of the BT474 cells and HUVECs. The gap between the pillar microstructures significantly affected the formation and size of the BT474 spheroids and the coverage of the HUVEC barriers on the liquid–hydrogel interfaces. Our approach has the potential to provide reliable and reproducible *in vitro* models for studying various biological processes, including drug development and delivery. Overall, the self-organized TME array-on-a-chip based on the integrative technology of bioprinting and microfluidics holds great promise for advancing the field of bioengineering.

Conflicts of interest

There are no conflicts to declare.

Acknowledgements

References

1 E. T. Roussos, J. S. Condeelis and A. Patsialou, *Nat. Rev. Cancer*, 2011, **11**, 573–587.

2 D. Wirtz, K. Konstantopoulos and P. C. Searson, *Nat. Rev. Cancer*, 2011, **11**, 512–522.

3 T. L. Whiteside, *Oncogene*, 2008, **27**, 5904–5912.

4 K. Gold, A. K. Gaharwar and A. Jain, *Biomaterials*, 2019, **196**, 2–17.

5 A. J. Primeau, A. Rendon, D. Hedley, L. Lilge and I. F. Tannock, *Clin. Cancer Res.*, 2005, **11**, 8782–8788.

6 S. Nath and G. R. Devi, *Pharmacol. Ther.*, 2016, **163**, 94–108.

7 M. T. Santini and G. Rainaldi, *Pathobiology*, 1999, **67**, 148–157.

8 X. Gong, C. Lin, J. Cheng, J. Su, H. Zhao, T. Liu, X. Wen and P. Zhao, *PLoS One*, 2015, **10**, e0130348.

9 S. Knowlton, S. Onal, C. H. Yu, J. J. Zhao and S. Tasoglu, *Trends Biotechnol.*, 2015, **33**, 504–513.

10 R. M. Thomas, T. Van Dyke, G. Merlino and C. P. Day, *Cancer Res.*, 2016, **76**, 5921–5925.

11 S. Kaneda, J. Kawada, M. Shinohara, M. Kumemura, R. Ueno, T. Kawamoto, K. Suzuki, B. Kim, Y. Ikeuchi, Y. Sakai, D. Collard, H. Fujita and T. Fujii, *Biomicrofluidics*, 2019, **13**, 054111.

12 S. Lee, H. Kang, D. Park, J. Yu, S. K. Koh, D. Cho, D. H. Kim, K. S. Kang and N. L. Jeon, *Adv. Biol.*, 2021, **5**, 2000195.

13 S. Pradhan, A. M. Smith, C. J. Garson, I. Hassani, W. J. Seeto, K. Pant, R. D. Arnold, B. Prabhakarpandian and E. A. Lipke, *Sci. Rep.*, 2018, **8**, 3171.

14 J. A. Hickman, R. Graeser, R. de Hoogt, S. Vidic, C. Brito, M. Gutekunst, H. van der Kuip and I. P. Consortium, *Biotechnol. J.*, 2014, **9**, 1115–1128.

15 J. Parrish, K. Lim, B. Zhang, M. Radisic and T. B. F. Woodfield, *Trends Biotechnol.*, 2019, **37**, 1327–1343.

16 E. W. Young, *Integr. Biol.*, 2013, **5**, 1096–1109.

17 P. Datta, M. Dey, Z. Ataie, D. Unutmaz and I. T. Ozbolat, *npj Precis. Oncol.*, 2020, **4**, 18.

18 B. Kwak, A. Ozcelikkale, C. S. Shin, K. Park and B. Han, *J. Controlled Release*, 2014, **194**, 157–167.

19 L. Wan, C. A. Neumann and P. R. LeDuc, *Lab Chip*, 2020, **20**, 873–888.

20 J. Ahn, Y. J. Sei, N. L. Jeon and Y. Kim, *Bioengineering*, 2017, **4**, 64.

21 Z. Hu, Y. Cao, E. A. Galan, L. Hao, H. Zhao, J. Tang, G. Sang, H. Wang, B. Xu and S. Ma, *ACS Biomater. Sci. Eng.*, 2022, **8**, 1215–1225.

22 Y. Lee, G. Lee, M. Cho and J.-K. Park, *J. Micromech. Microeng.*, 2019, **29**, 043003.

23 G. Lee, S. J. Kim, H. Chun and J.-K. Park, *Biofabrication*, 2021, **13**, 045027.

24 Y. S. Zhang, M. Duchamp, R. Oklu, L. W. Ellisen, R. Langer and A. Khademhosseini, *ACS Biomater. Sci. Eng.*, 2016, **2**, 1710–1721.

25 D. B. Kolesky, K. A. Homan, M. A. Skylar-Scott and J. A. Lewis, *Proc. Natl. Acad. Sci. U. S. A.*, 2016, **113**, 3179–3184.

26 M. Dey, M. H. Kim, M. Dogan, M. Nagamine, L. Kozhaya, N. Celik, D. Unutmaz and I. T. Ozbolat, *Adv. Funct. Mater.*, 2022, **32**, 2270296.

27 J. Li, C. Parra-Cantu, Z. Wang and Y. S. Zhang, *Trends Cancer*, 2020, **6**, 745–756.

28 J. Y. Park, J. Jang and H.-W. Kang, *Microelectron. Eng.*, 2018, **200**, 1–11.

29 H. G. Yi, Y. H. Jeong, Y. Kim, Y. J. Choi, H. E. Moon, S. H. Park, K. S. Kang, M. Bae, J. Jang, H. Youn, S. H. Paek and D. W. Cho, *Nat. Biomed. Eng.*, 2019, **3**, 509–519.

30 Y. S. Zhang, A. Arneri, S. Bersini, S. R. Shin, K. Zhu, Z. Goli-Malekabadi, J. Aleman, C. Colosi, F. Busignani, V. Dell'Erba, C. Bishop, T. Shupe, D. Demarchi, M. Moretti, M. Rasponi, M. R. Dokmeci, A. Atala and A. Khademhosseini, *Biomaterials*, 2016, **110**, 45–59.

31 J. U. Lind, T. A. Busbee, A. D. Valentine, F. S. Pasqualini, H. Yuan, M. Yadid, S. J. Park, A. Kotikian, A. P. Nesmith, P. H. Campbell, J. J. Vlassak, J. A. Lewis and K. K. Parker, *Nat. Mater.*, 2017, **16**, 303–308.

32 S. J. Kim, G. Lee and J.-K. Park, *Adv. Mater. Technol.*, 2021, **7**, 2101326.

33 S. Knowlton, A. Joshi, B. Yenilmez, I. T. Ozbolat, C. K. Chua, A. Khademhosseini and S. Tasoglu, *Int. J. Bioprint.*, 2016, **2**, 3–8.

34 H. Seo, J. Son and J.-K. Park, *APL Bioeng.*, 2020, **4**, 046103.

35 A. Aung, J. Theprungsirikul, H. L. Lim and S. Varghese, *Lab Chip*, 2016, **16**, 1886–1898.

36 X. Cui, Y. Hartanto and H. Zhang, *J. R. Soc., Interface*, 2017, **14**, 20160877.

37 S. Kim, S. Kwon, C. H. Cho and J.-K. Park, *Lab Chip*, 2017, **17**, 702–709.

38 C. H. Cho, M. Cho and J.-K. Park, *Lab Chip*, 2021, **21**, 3471–3482.

39 C. P. Huang, J. Lu, H. Seon, A. P. Lee, L. A. Flanagan, H.-Y. Kim, A. J. Putnam and N. L. Jeon, *Lab Chip*, 2009, **9**, 1740.

40 G. Lee, S. J. Kim and J.-K. Park, *STAR Protoc.*, 2022, **3**, 101303.